

Metal–support frontier orbital interactions in single-atom catalysis

<https://doi.org/10.1038/s41586-025-08747-z>

Received: 29 July 2022

Accepted: 6 February 2025

Published online: 2 April 2025

 Check for updates

Xianxian Shi^{1,2,3,9}, Zhilin Wen^{2,9}, Qingqing Gu^{4,9}, Long Jiao^{1,2}, Hai-Long Jiang^{1,2}, Haifeng Lv¹, Hengwei Wang¹, Jian Ding^{1,2}, Mason P. Lyons⁵, Alvin Chang⁶, Zhenxing Feng⁵, Si Chen², Yue Lin¹, Xiaoyan Xu⁴, Pengfei Du⁴, Wenlong Xu², Mei Sun¹, Yin Li², Bing Yang^{4,✉}, Tao Zhang⁴, XIAOJUN WU^{1,2,7,✉} & Junling Lu^{1,2,8,✉}

Single-atom catalysts (SACs) with maximized metal use and discrete energy levels hold promise for broad applications in heterogeneous catalysis, energy conversion, environmental science and biomedicine^{1–7}. The activity and stability of SACs are governed by the pair of metal–adsorbate and metal–support interactions^{8–10}. However, the understanding of these interactions with their catalytic performance in nature is challenging. Correlations of activity with the charge state of metal atoms have frequently reached controversial conclusions^{11–15}. Here we report that the activity of palladium (Pd_1) SACs exhibits a linear scaling relationship with the positions of the lowest unoccupied molecular orbital (LUMO) of oxide supports across 14 types of semiconductor. Elevation of the LUMO position by reducing the support particle size to a few nanometres boosts a record high activity along with excellent stability in the semi-hydrogenation of acetylene. We show that the elevated LUMO of support reduces its energy gap with the highest occupied molecular orbital (HOMO) of Pd_1 atoms, which promotes Pd_1 –support orbital hybridizations for high stability and further amends the LUMO of anchored Pd_1 atoms to enhance Pd_1 –adsorbate interactions for high activity. These findings are consistent with the frontier molecular orbital theory and provide a general descriptor for the rational selection of metal–support pairs with predictable activity.

Metal–support interactions (MSIs) in single-atom catalysts (SACs) often induce substantial electronic perturbations to the metal^{16,17}, the so-called electronic MSI (EMSI)^{18,19}. The charge state of metal atoms inferred from X-ray photoelectron spectroscopy (XPS), X-ray absorption near-edge structure and infrared vibrational spectroscopy has often been used to depict the strength of EMSI and to explain the catalytic activity^{11,12,20–22}. However, it leads to intensive debates on which charge state of metal atoms is catalytically more active^{11–15}. Meanwhile, the character of discrete energy structures of SACs also raises questions about the *d*-band theory, which is widely adopted for metal nanoparticle catalysts with continuous energy band structures²³. Alternatively, frontier molecular orbital (FMO) theory, frequently applied to homogeneous molecular catalysts^{24,25}, has also been advocated to depict M_1 –adsorbate orbital interactions in SACs^{8–10,26}. However, the panoramic illustration of M_1 –support and M_1 –adsorbate orbital interactions in SACs has not yet been demonstrated either theoretically or experimentally to the best of our knowledge. Fundamental questions about the nature of these interactions in single-atom catalysis remain unanswered.

To obtain a deep insight of these interactions, we synthesized 34 Pd_1 SACs across 14 types of semiconducting support, in which the size

of supports was also tuned to further modulate their electronic band structures (Fig. 1a). First, a series of semiconducting oxide particles ($MO_x = ZnO, CoO_x, NiO_x, TiO_2$ and Ga_2O_3 with varied sizes) were grown on a spherical SiO_2 substrate using atomic layer deposition (ALD) by varying the number of ALD cycles²⁷ (Supplementary Figs. 1–6). These supports are denoted as MO_x –y nm, where y is the average size of oxide particles. Ultraviolet–visible (UV–Vis) spectroscopy and Mott–Schottky plots measurements^{28,29} showed that the n-type bulk ZnO has the lowest unoccupied molecular orbital (LUMO) position of -0.35 V (versus normal hydrogen electrode (NHE)), and a band gap (E_g) of 3.29 eV (Fig. 1b and Supplementary Figs. 7 and 8). As the size of ZnO decreased from bulk (about 46 nm) to about 1.9 nm, the LUMO position upshifted gradually to -1.12 V (versus NHE), and the band gap became considerably broader to 5.82 eV (Supplementary Figs. 9 and 10), in good agreement with the literature²⁸. Similar phenomena were also observed for other MO_x particles, regardless of whether they were n- or p-type semiconductors³⁰ (Fig. 1b, Supplementary Figs. 11–20 and Supplementary Table 1). Therein, the upshift of LUMO positions is big for p-type CoO_x samples, but small for NiO_x, TiO_2 and Ga_2O_3 with the change of particle size.

¹State Key Laboratory of Precision and Intelligent Chemistry, Hefei National Research Center for Physical Sciences at the Microscale, University of Science and Technology of China, Hefei, China.

²School of Chemistry and Materials Science, iChem, University of Science and Technology of China, Hefei, China. ³College of Aerospace Science and Engineering, National University of Defense Technology, Changsha, China. ⁴CAS Key Laboratory of Science and Technology on Applied Catalysis, Dalian Institute of Chemical Physics, Chinese Academy of Sciences, Dalian, China. ⁵School of Chemical, Biological, and Environmental Engineering, Oregon State University, Corvallis, OR, USA. ⁶School of Mechanical, Industrial, and Manufacturing Engineering, Oregon State University, Corvallis, OR, USA. ⁷Hefei National Laboratory, University of Science and Technology of China, Hefei, China. ⁸Suzhou Laboratory, Suzhou, China. ⁹These authors contributed equally: Xianxian Shi, Zhilin Wen, Qingqing Gu. [✉]e-mail: byang@dicp.ac.cn; xjwu@ustc.edu.cn; junling@ustc.edu.cn

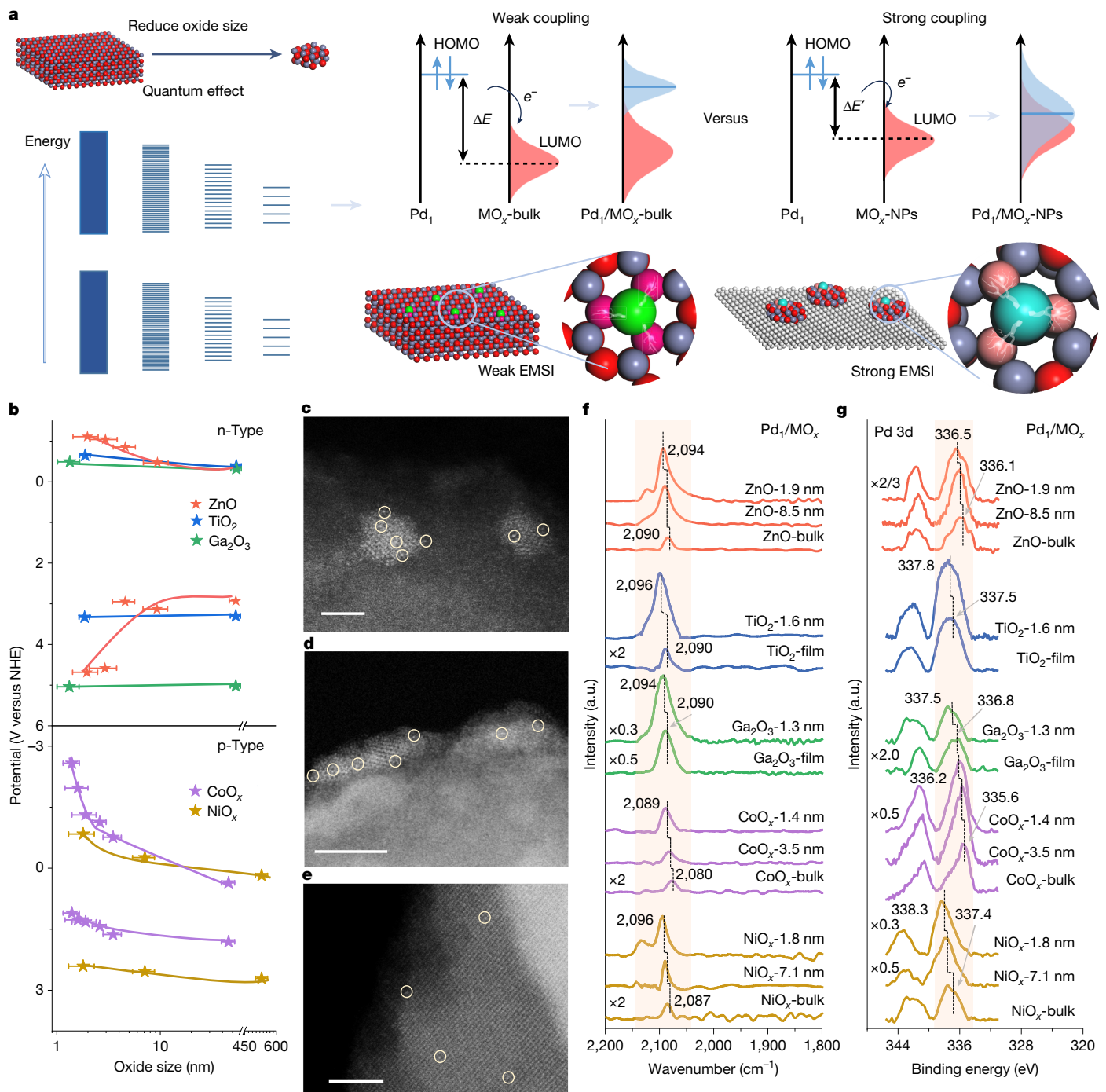


Fig. 1 | Variation of EMSIs in Pd_1/MO_x SACs on support particle size.

a, Schematic of tailoring EMSIs in Pd_1/MO_x SACs by changing the energy band structures of oxide supports by size variation. **b**, Energy-level diagrams of n- and p-type metal oxides with different particle sizes as determined by TEM, UV-Vis and Mott-Schottky plots. Here the size of the spherical SiO_2 substrate was used to represent the size of the TiO_2 and Ga_2O_3 films grown on top. Error bars represent the standard deviations of oxide particle size as determined by

TEM. **c–e**, Representative AC-HAADF-STEM images of Pd_1/ZnO -1.9 nm (**c**), Pd_1/ZnO -8.5 nm (**d**) and Pd_1/ZnO -bulk (**e**). The white circles in **c–e** highlight Pd_1 single atoms on ZnO . **f,g**, In situ DRIFTS CO chemisorption (**f**) and in situ XPS spectra (**g**) in the $\text{Pd} 3d$ region of Pd_1/MO_x SACs. All samples were pre-reduced at 100°C for 30 min with 10 vol% H_2/Ar before CO chemisorption and XPS measurements without exposure to air. Scale bars, 2 nm (**c,e**); 5 nm (**d**).

Next, Pd_1 atoms were selectively deposited on MO_x particles using Pd ALD to obtain a series of Pd_1/MO_x SACs, in which the selective deposition was confirmed by inductively coupled plasma atomic emission spectroscopy (ICP-AES) analysis (Supplementary Fig. 21). Pd_1 atoms were also deposited on some bulk oxide supports (Pd_1/MO_x -bulk) for comparison. The Pd loadings in Pd_1/MO_x were all close to 0.1 wt% according to ICP-AES (Supplementary Table 2). Aberration-corrected high-angle annular dark-field scanning transmission electron

microscopy (AC-HAADF-STEM) confirmed the atomic dispersion of Pd without the presence of any visible clusters or nanoparticles in all these samples (Fig. 1c–e and Supplementary Figs. 22–26). DRIFTS of CO chemisorption also showed that all Pd_1/MO_x -y nm samples exhibited a single peak at $2,080$ – $2,096 \text{ cm}^{-1}$, assigned to linear CO on Pd_1 atoms³¹ (Fig. 1f), but with the absence of bridge-bonded CO (about $1,900$ – $2,000 \text{ cm}^{-1}$), further validating the atomic dispersion of Pd . We observed blueshifts of CO peak by a few wavenumbers in all sets

Article

of Pd₁ SACs as the size of oxide supports decreased, suggesting that Pd₁ atoms on nanosized oxide particles were more electron deficient, weakening the Pd(4d)-CO(2π*) bonding through π back-donation³². In situ XPS also demonstrated the shifts of Pd 3d peak to higher binding energies by about 0.3–0.9 eV across all sets of samples (Fig. 1g), confirming the increased electron deficiency of Pd₁ atoms. UV–Vis spectra also disclosed more significant changes of the ZnO band structures in Pd₁/ZnO-1.9 nm and Pd₁/ZnO-2.8 nm than that in Pd₁/ZnO-bulk by Pd deposition (Supplementary Fig. 27). Consequently, the above results all indicate the greatly enhanced orbital hybridizations between Pd₁ and nanosized oxide particles.

The semi-hydrogenation of acetylene in excess ethylene, an industrial process for purifying alkene streams³³, was used as a probe reaction to evaluate their performance. We found that at a high acetylene conversion of 90%, the ethylene selectivity of these catalysts all remained above 90%, except for slightly lower ethylene selectivity on Pd₁/Ga₂O₃-film and Pd₁/TiO₂-film (Supplementary Figs. 28–32). However, the intrinsic activity in terms of turnover frequencies (TOFs) per Pd atom increased substantially as the oxide particle size decreased (Fig. 2a). For the set of Pd₁/ZnO-*y* nm SACs, the TOF was approximately 25.6 min⁻¹ for Pd₁/ZnO-1.9 nm at 80 °C, far superior to the conventional Pd₁/ZnO-bulk catalyst (1.0 min⁻¹) (Supplementary Fig. 28). A tremendous activity enhancement was also observed for Pd₁/CoO_x-*y* nm with the TOFs increased dramatically from 1.0 min⁻¹ to 22.6 min⁻¹ (Supplementary Fig. 29), whereas the sets of Pd₁/NiO_x, Pd₁/Ga₂O₃ and Pd₁/TiO₂ catalysts showed relatively smaller activity enhancements (Supplementary Figs. 30–32).

Kinetic studies showed that the apparent reaction barriers (E_a) decreased considerably for all sets of Pd₁ SACs as the oxide particle size decreased (Supplementary Fig. 33), verifying the remarkable activity improvement. It is worth noting that the activity of Pd₁/ZnO-1.9 nm is far superior to those Pd₁ SACs reported in the literature^{34,35} and in particular approximately 46 times greater than the benchmark Pd₁/Ag/SiO₂ single-atom alloy catalyst³⁵ (Fig. 2b and Supplementary Table 3). More importantly, Pd₁/ZnO-1.9 nm also exhibited excellent stability without any noticeable decrease in either activity or selectivity for at least 100 h (Fig. 2c). By contrast, Pd₁/ZnO-8.5 nm and Pd₁/ZnO-bulk both deactivated rapidly along with a continuous decrease in ethylene selectivity. HAADF-STEM imaging showed that Pd atoms remained atomically dispersed in the used Pd₁/ZnO-1.9 nm and Pd₁/ZnO-8.5 nm catalysts after the long-term reaction, whereas severe aggregations occurred in the used Pd₁/ZnO-bulk catalyst (Supplementary Fig. 34). In situ thermogravimetric analysis under hydrogenation conditions showed that coke deposition, another key factor of catalyst deactivation³³, was also negligible on Pd₁/ZnO-1.9 nm, but substantially on Pd₁/ZnO-8.5 nm and Pd₁/ZnO-bulk (Supplementary Fig. 35). Pd₁/ZnO-1.9 nm also showed enhanced activity and long-term stability in the selective hydrogenation of 1,3-butadiene (Supplementary Fig. 36), rendering this material promising for a wide range of selective hydrogenation reactions.

Correlation of the intrinsic activities with the properties of Pd₁ discloses that the activities of Pd₁/MO_x SACs showed a tight linear correlation with the Pd charge states in each series of samples (Fig. 2d), in line with the literature^{11,12,22}. However, this relation failed when the activities of all sets of samples were compared. By contrast, their activities showed a linear scaling relationship with the LUMO positions of the n- and p-type oxide particle supports in Pd₁/MO_x (Fig. 2e,f). To confirm the above linear scaling, 16 more Pd₁ SACs on various bulk semiconducting supports (n-type: ZrO₂, ZnAl_xO_y, SrTiO₃, Fe₃O₄, Fe₂O₃ and MgAl_xO_y with different Al to Mg ratios, and InO_x with varied sizes; and p-type: Cu₂O and CuO) were further synthesized and evaluated (Supplementary Figs. 37–46). Their activities were again in a good fit of the above linear scaling, implying the essential role of the LUMO positions of oxide particles in governing the activity of Pd₁ SACs (Fig. 2e,f and Supplementary Figs. 42–46). This result is in line with the observation of a linear

correlation between the C–H activation energy and the surface reducibility of metal oxides in ref. 36, because the oxygen vacancy formation energy is probably associated with the LUMO position of oxide^{28,29}. Here, compared with that for the p-type ones, a steeper slope for the n-type samples, along with relatively larger deviations from the fittings is noticed, which is probably caused by the perturbations from impurity energy levels that are close to the LUMOs of n-type semiconductors³⁰. We also measured the LUMO positions of several representative supports using ultraviolet photoelectron spectroscopy (Supplementary Fig. 47 and Supplementary Table 4) and UV–Vis (Supplementary Figs. 9, 42–44). It again showed a similar linear scaling relationship, validating the above results (Supplementary Figs. 48 and 49 and Supplementary Tables 5 and 6).

H₂ activation is a crucial step in SAC-catalysed hydrogenation reactions¹¹. We demonstrated that as the oxide particle size decreased, the H–D exchange rates over these Pd₁ SACs also increased greatly in the H–D exchange reaction (Fig. 3a), which was further confirmed by kinetic measurements (Supplementary Fig. 50). These results indicate that the drastic improvement in hydrogenation activity in Fig. 2a can be attributed to the facilitation of H₂ activation. More interestingly, a linear scaling relationship between the LUMO positions of either n- or p-type oxide supports and the activities of Pd₁ SACs was again established (Fig. 3b).

Temperature-programmed desorption (TPD) of H₂ on selected Pd₁/ZnO-*y* nm showed that there were two H₂ desorption peaks located at 46 °C and 362 °C for Pd₁/ZnO-bulk (Fig. 3c), assigned to chemisorbed H₂ on Pd₁ atoms and spillover H₂ on the ZnO support, respectively³⁷; the latter case is further confirmed by the observation of noticeable surface hydroxyls formation after H₂ exposure using in situ XPS (Supplementary Fig. 51). As the size of ZnO decreased, the H₂ desorption peak from Pd₁ atoms gradually shifted to 87 °C. Meanwhile, the C₂H₂ desorption temperature also shifted from 52 °C to 109 °C accordingly (Fig. 3d). Here the increased H₂ desorption temperature remained lower than that of C₂H₂, which is consistent with the decreased H₂ reaction order and negative C₂H₂ reaction order on Pd₁/ZnO-1.9 nm (Supplementary Fig. 52). The reduction of the underlying ZnO particle size to a few nanometres endows the Pd₁ atoms to be more electron deficient (Fig. 1f,g), which in turn enhances the adsorption of H₂ and C₂H₂ on Pd. Moreover, we also noticed that the peak area of C₂H₂ desorption on Pd₁/ZnO-1.9 nm became substantially larger owing to additional C₂H₂ adsorption on support (Supplementary Fig. 53). Nonetheless, ZnO-1.9 nm itself was inactive, and the H₂ spillover effect on activity was trivial (Supplementary Fig. 54).

To understand the linear scaling relationship as well as improved stability, density functional theory (DFT) calculations were further performed on the Pd₁/ZnO system, in which ZnO slab and clusters with different numbers of units (ZnO-*x*, where *x* is the number of units) and all nonpolar (10̄10̄) surface exposed were calculated to represent the ZnO bulk and particles with different sizes. Calculations using the Perdew–Burke–Ernzerhof (PBE) exchange-correlation functional show that the HOMO position of freestanding Pd₁ atom is located at -4.08 eV (Fig. 4a), whereas the LUMO and HOMO of ZnO slab are located at -5.46 eV and -5.68 eV, respectively (Supplementary Fig. 55). As ZnO particle size is reduced to ZnO-30, the LUMOs sharply climb to -4.32 eV, whereas their HOMOs decline, which together broaden the band gap, consistent with the experimental results (Fig. 1b). It is worth noting that the PBE functional might have considerably underestimated the band gap, although the trend of changes in the LUMO positions can be reliable and further corroborated by calculations using a high-level screened hybrid Heyd–Scuseria–Ernzerhof (HSE06) functional (Supplementary Table 7). The reduction of ZnO particle size largely narrows the energy gap between the LUMO of ZnO and the HOMO of freestanding Pd atom. According to the FMO theory^{24,25}, this would substantially intensify orbital couplings between these two to lead to a high stability (Fig. 1a).

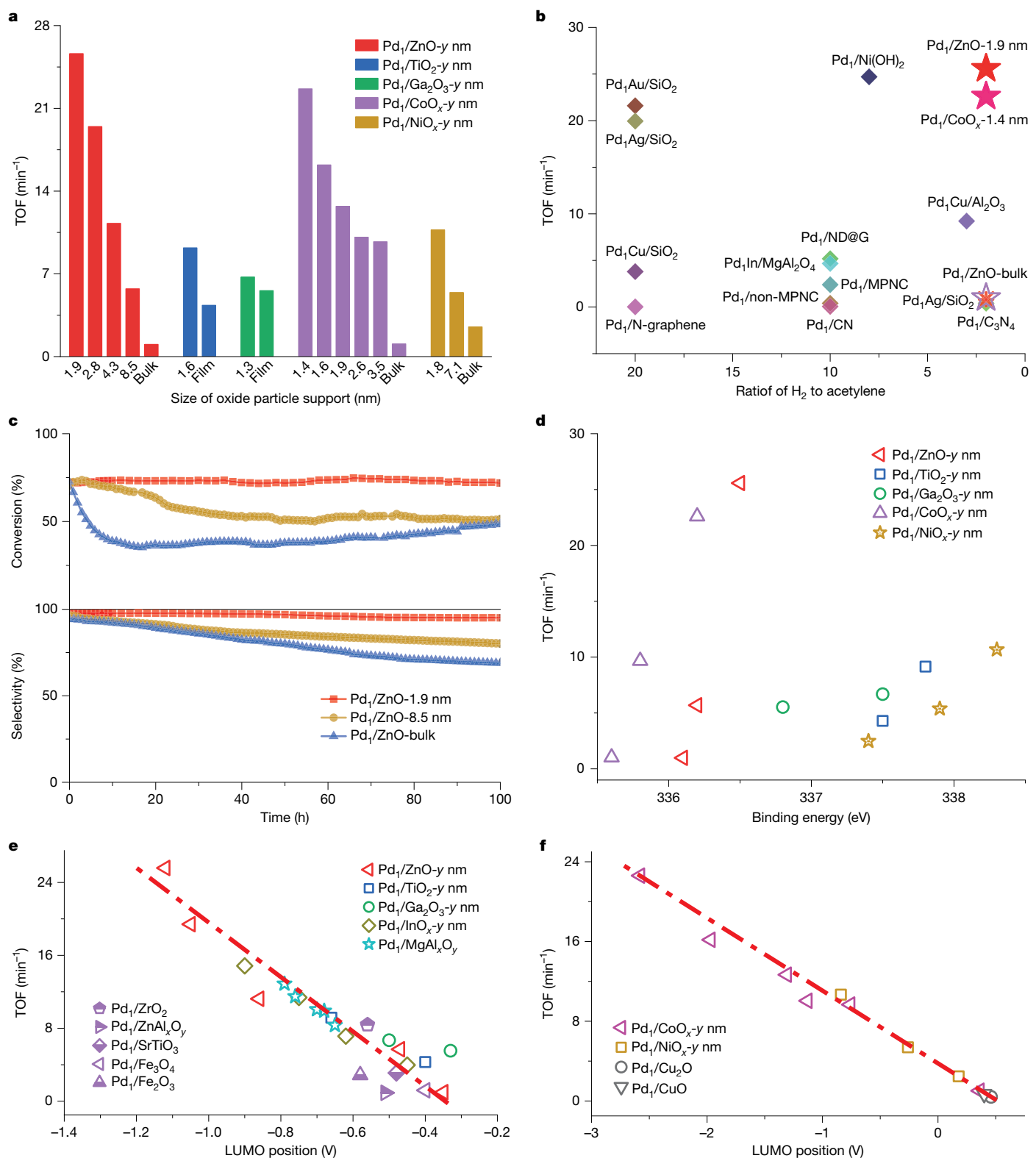


Fig. 2 | Catalytic performance of Pd₁/MO_x catalysts. **a**, Intrinsic activities of Pd₁/MO_x catalysts at 80 °C in the semi-hydrogenation of acetylene in excess ethylene. **b**, Comparison of the activities of Pd₁/ZnO-1.9 nm and Pd₁/CoO_x-1.4 nm with those of conventional Pd-based SACs reported in the literature at 80 °C. **c**, Acetylene conversion and ethylene selectivity as a function of time during long-term stability tests of Pd₁/ZnO-1.9 nm, Pd₁/ZnO-8.5 nm and Pd₁/ZnO-bulk.

The optimized structures of Pd₁ on ZnO show preferential anchoring of Pd₁ atoms at Zn vacancies with three Pd–O coordinations (Supplementary Fig. 56 and Supplementary Table 8), evidenced by X-ray

absorption spectroscopy (Supplementary Fig. 57 and Supplementary Table 9) and high-resolution HAADF-STEM measurements (Supplementary Fig. 22). The adsorption of Pd₁ on nanosized ZnO is

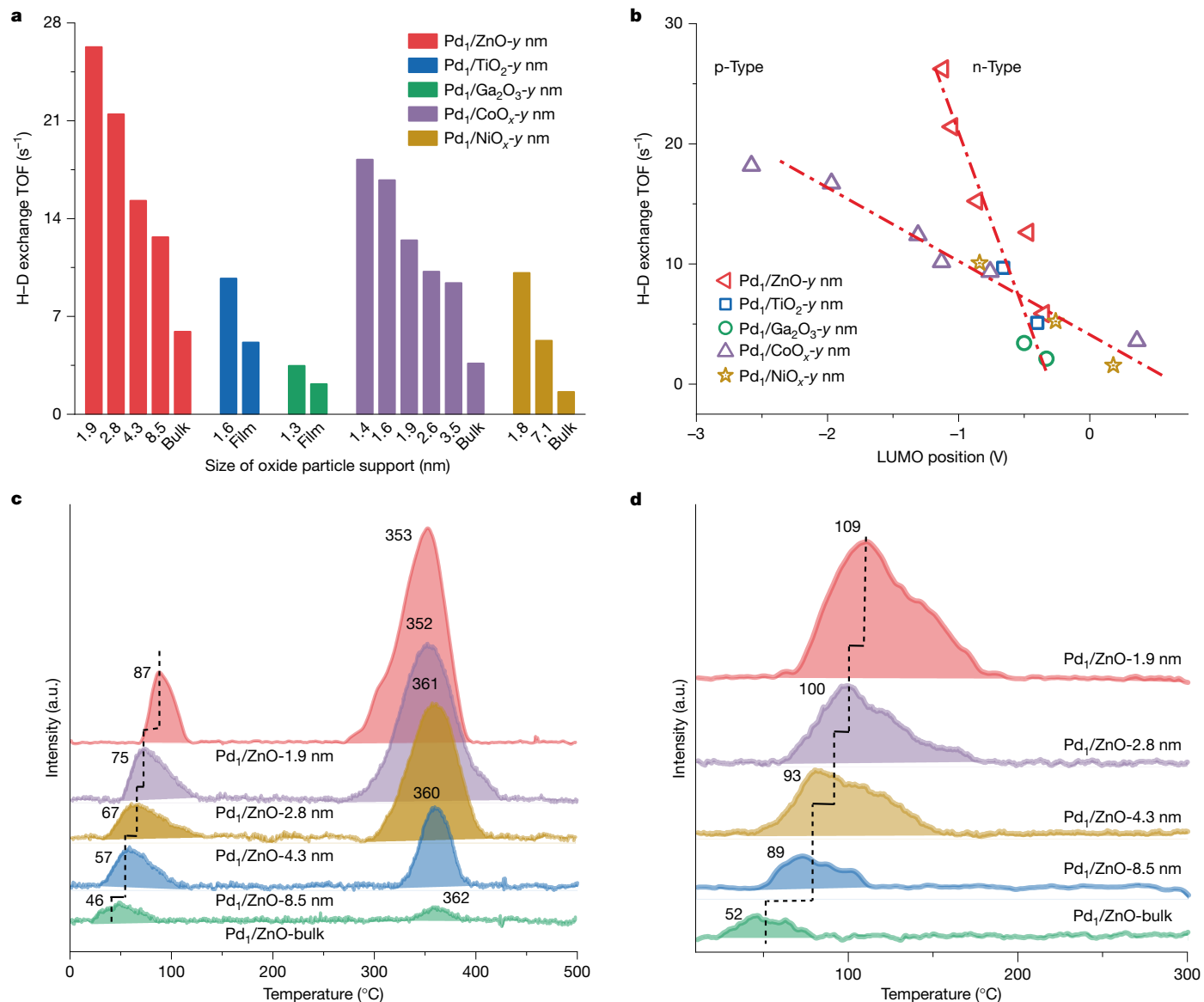


Fig. 3 | Chemical properties of Pd₁/MO_x SACs. **a**, The H–D exchange rates of Pd₁/MO_x SACs at 80 °C. **b**, Linear scaling relationships between the H–D exchange activity and the LUMO positions of n- and p-type semiconducting oxide supports. **c,d**, TPD curves of H₂ (**c**) and acetylene (**d**) over various Pd₁/ZnO-y nm catalysts.

considerably stronger than on ZnO-slab (Supplementary Table 10). Charge density difference analysis further illustrates markedly stronger orbital couplings along with greater charge transfer from Pd₁ atom to nanosized ZnO in Pd₁/ZnO-x (Fig. 4a (inset) and Supplementary Figs. 58 and 59), consistent with the DRIFTS CO chemisorption and XPS results (Fig. 1f,g). These results verify the high stability of Pd₁/ZnO-1.9 nm. When electrons are transferred from Pd to ZnO, the original HOMO of freestanding Pd₁ atoms becomes an unoccupied or partially occupied state (or LUMO) of anchored Pd₁ atoms in Pd₁/ZnO. Therefore, intensifying Pd₁-ZnO orbital coupling would enhance charge transfer and cause a greater downshift and broadening of Pd energy levels (Supplementary Fig. 60 and Supplementary Note), which in turn leads to the lowering of the LUMO position of anchored Pd₁ atoms. Deconvoluted partial density of states (PDOS) analysis demonstrates this gradual decline for Pd₁/ZnO-x (mainly contributed by the $d_{x^2-y^2}$ orbitals of Pd) with the reduction of ZnO particle size (Fig. 4b and Supplementary Fig. 61), analogous to the ligand effect in homogeneous catalysts³⁸.

Regarding the M₁-adsorbate orbital interactions, we show that the lowered LUMO of Pd₁ atoms on nanosized ZnO exhibits smaller energy

gaps with the HOMOs of C₂H₂ (mainly contributed by the p_y and p_x orbitals of C₂H₂) and H₂ molecules (Fig. 4c), which could reinforce the Pd₁-adsorbate orbital overlapping and enhance their adsorption according to the FMO theory^{24,25} (Fig. 4c). As the ZnO particle size decreases from ZnO-slab to ZnO-30, the adsorption energies of H₂ and C₂H₂ on Pd₁ increase substantially from 0.30 eV to -0.84 eV and from -0.38 eV to -1.61 eV, respectively (Fig. 4d), in line with the TPD results (Fig. 3c,d).

Next, we calculated the energy profiles for H₂ activation and C₂H₂ hydrogenation on Pd₁/ZnO-52 (the size of ZnO-52 is close to that in Pd₁/ZnO-1.9 nm) and Pd₁/ZnO-slab. We demonstrate that compared with Pd₁/ZnO-slab, Pd₁ in Pd₁/ZnO-52 draws more electrons from the bonding orbitals of H₂ molecule owing to the increased electron deficiency (Supplementary Fig. 62), which enhances its adsorption (-0.43 eV) and facilitates sequential H–H bond activation (energy barrier of 0.46 eV versus 1.03 eV; Supplementary Fig. 63), consistent with the H–D exchange results (Fig. 3a). In C₂H₂ hydrogenation (Fig. 4e, Supplementary Fig. 64 and Supplementary Tables 11 and 12), we show that on Pd₁/ZnO-52, C₂H₂ first adsorbs on the Pd₁ atom (Fig. 4e, i, ii). Then, H₂ approaches the Pd₁ and dissociates heterolytically with a low

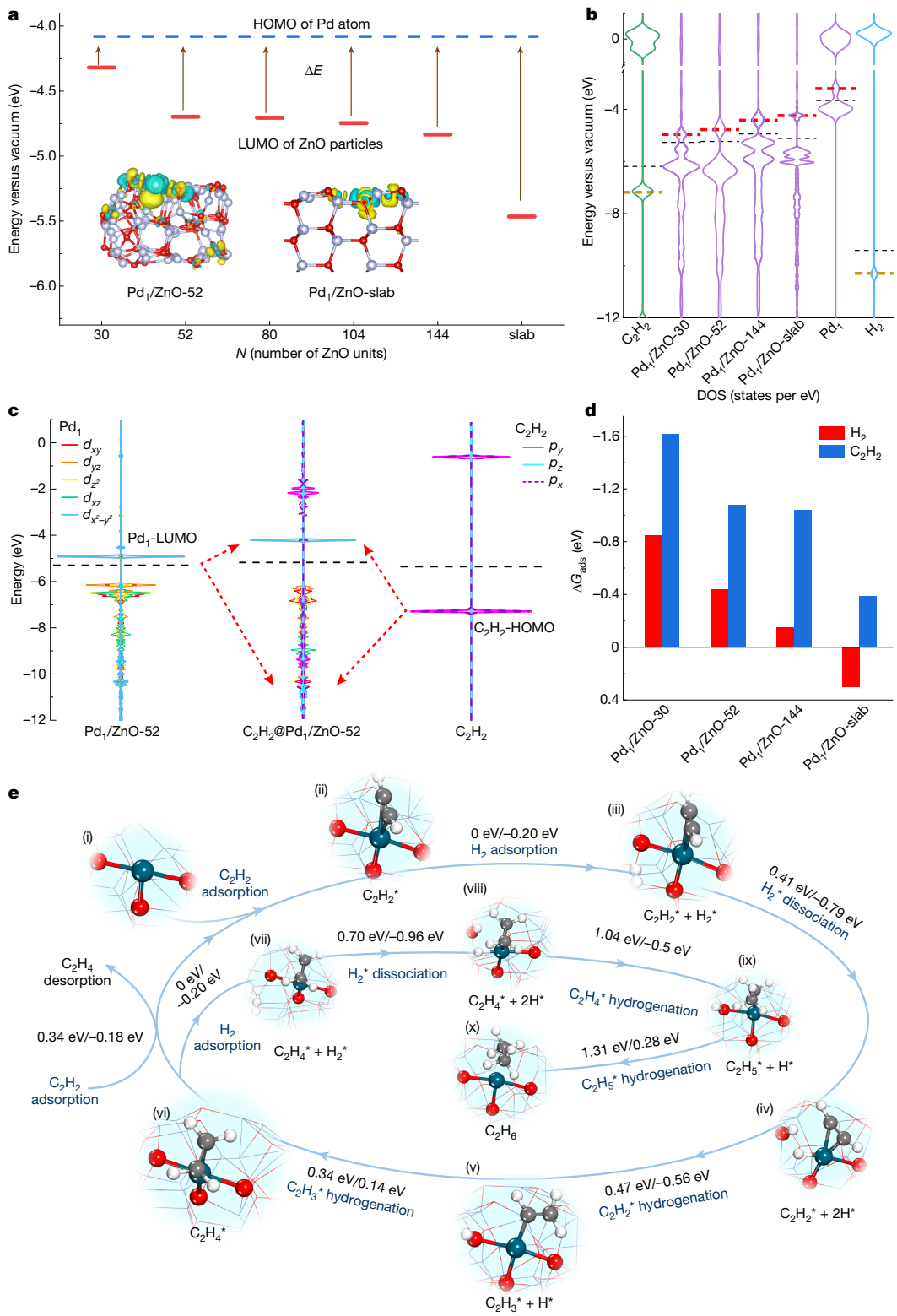


Fig. 4 | Theoretical insight into orbital coupling on activity in Pd₁/ZnO SACs. **a**, Calculated LUMO positions of ZnO particles with different sizes (red horizontal solid line) and the HOMO of unsupported Pd₁ atom (blue dashed horizontal line) relative to vacuum. Shiny brown arrows highlight the energy discrepancies (ΔE) between the ZnO LUMOs and the Pd₁ HOMO. The insets in **a** show the charge density difference of Pd₁ atoms in Pd₁/ZnO-52 and Pd₁/ZnO-slab, in which the yellow and cyan regions represent electron accumulation and electron depletion, respectively. The isosurface value is 0.002e Bohr⁻³ (ref. 3). **b**, PDOSs of unsupported and ZnO-x-supported Pd₁ with varying ZnO sizes. The PDOSs of C₂H₂ and H₂ in the gas state are also given here for comparison.

The red and brown horizontal dashed lines indicate the LUMOs of unsupported and ZnO-x-supported Pd₁ and the HOMOs of C₂H₂ and H₂, respectively. **c**, PDOS analysis of orbital interactions between Pd₁/ZnO-52 and C₂H₂ molecule before and after adsorption. **d**, Calculated adsorption free energies of H₂ and C₂H₂ on Pd₁/ZnO-x with different ZnO particle sizes. **e**, Calculated Gibbs free energy profiles of selective hydrogenation of acetylene on Pd₁/ZnO-52. The structures of the key steps and intermediates are shown, as well as the energy barriers (left of the slash) and reaction free energies (right of the slash) between the corresponding key steps. Here, Pd, O, C, H and Zn atoms are in cyan, red, grey, white and silver, respectively.

barrier of 0.41 eV (Fig. 4e, iii → iv). In the following, the two H^{*} (asterisk denotes surface species) sequentially attack C₂H₂^{*} to form C₂H₄^{*}, with barriers of only 0.47 eV and 0.35 eV, respectively (Fig. 4e, iv → vi). Next, C₂H₄^{*} desorbs easily with a low barrier of 0.34 eV with the assistance of competitive C₂H₂ adsorption (Supplementary Fig. 65), evidenced by the slight increase in the C₂H₂ reaction order after introducing ethylene to the reaction gas (Supplementary Fig. 52). Here the first addition of H^{*} to C₂H₂^{*} to form C₂H₃^{*} is the rate-limiting step. Further hydrogenation of C₂H₄^{*} to C₂H₆^{*} is highly unfavourable, with a considerably high barrier of 1.31 eV (Fig. 4e, vii → x). For Pd₁/ZnO-slab, the hydrogenation of C₂H₂ becomes considerably laborious (Supplementary Figs. 64, 66 and 67), in which the H^{*} attack of C₂H₂^{*} to form C₂H₃^{*} has a barrier as high as 0.84 eV. Microkinetic simulations further confirmed the much greater activity of Pd₁/ZnO-52 than of Pd₁/ZnO-slab (Supplementary Fig. 68), agreeing well with the experimental results (Fig. 2a). Here, the improved activity is mainly attributed to the greatly enhanced H₂ adsorption and activation (Fig. 2b, Supplementary Fig. 69 and Supplementary Table 13).

Notably, the variations in the Pd coordination structures (for example, Pd–O bond lengths and O–Pd–O bond angles), which are due to variations in the ZnO facet orientations and anchoring sites on the ZnO clusters, do not alter the above result (Supplementary Figs. 70 and 71 and Supplementary Tables 14 and 15). Hydroxyls and oxygen vacancies might also be present on ZnO surfaces but have a minor effect on the activity (Supplementary Figs. 72–75 and Supplementary Tables 16–20).

Calculations were also carried out on the Pd₁/Ga₂O₃ and Pd₁/Co₃O₄ systems. We show that the variation of Ga₂O₃ size upshifts only its LUMO position slightly from −5.23 eV to −4.90 eV ($\Delta(\text{LUMO}) = 0.33 \text{ eV}$), which causes minor changes in the adsorption of adsorbates on various Pd₁/Ga₂O₃ (Supplementary Figs. 76 and 77 and Supplementary Tables 21 and 22). By contrast, the upshift of the Co₃O₄ LUMO is relatively large ($\Delta(\text{LUMO}) = 0.78 \text{ eV}$), close to the change in the ZnO LUMO ($\Delta(\text{LUMO}) = 1.14 \text{ eV}$) as its size decreases from the bulk to a Co₁₁O₁₃ cluster, which further leads to considerably enhanced adsorption of adsorbates on Pd₁/Co₁₁O₁₃ (Supplementary Figs. 78 and 79 and Supplementary Tables 23 and 24). These calculation results agree well with the small activity improvement on the set of Pd₁/Ga₂O₃-y nm SACs but large improvement on Pd₁/CoO_x-y nm (Fig. 2a), again unambiguously verifying the essential roles of the LUMO positions of semiconducting supports in single-atom catalysis.

Finally, to gain insight into the failure in the correlation of the activities with the Pd charge states across various supports (Fig. 2d), we further calculated the average ionicity of Pd–O bonds on several oxide supports according to natural bond orbital analysis³⁹. We show that the ionicities of Pd–O bonds in average for Pd₁/ZnO-52 and Pd₁/ZnO-slab are rather close to each other, approximately 64.1% and 67.3%, respectively, but change substantially from one oxide to another, approximately 81.1%, 66.2%, 52.1%, 75.6%, 67.2% and 71.7% for Co₃O₄, TiO₂, Ga₂O₃, NiO, CuO and ZrO₂, respectively (Supplementary Fig. 80 and Supplementary Table 25). It demonstrates that ionic and covalent bonding are capricious with the type of support, in line with the literature¹⁶, thus excluding the charge states of metal atom as a unified descriptor for the activity of SACs across various supports. In line with this observation, both experiments and theory demonstrate that although the higher charge state of Pd₁ atoms in Pd₁/Ga₂O₃ than that of Pd₁/ZnO-1.9 nm (Figs. 1f,g, Supplementary Fig. 81 and Supplementary Table 26), Pd₁/Ga₂O₃ shows a considerably lower activity (Figs. 2d and 3a and Supplementary Figs. 50 and 82).

In summary, the identification of the measurable LUMO positions of both n- and p-type semiconducting supports as a universal descriptor for the predictable activity and stability of SACs substantiates the FMO theory experimentally. More importantly, these findings also open a new avenue with high practicability for screening proper

metal–support pairs for high activity and stability, particularly when powered by artificial intelligence⁴⁰.

Online content

Any methods, additional references, Nature Portfolio reporting summaries, source data, extended data, supplementary information, acknowledgements, peer review information; details of author contributions and competing interests; and statements of data and code availability are available at <https://doi.org/10.1038/s41586-025-08747-z>.

- Wang, A., Li, J. & Zhang, T. Heterogeneous single-atom catalysis. *Nat. Rev. Chem.* **2**, 65–81 (2018).
- Kaiser, S. K. et al. Single-atom catalysts across the periodic table. *Chem. Rev.* **120**, 11703–11809 (2020).
- Hulva, J. et al. Unraveling CO adsorption on model single-atom catalysts. *Science* **371**, 375–379 (2021).
- Flytzani-Stephanopoulos, M. Gold atoms stabilized on various supports catalyze the water–gas shift reaction. *Acc. Chem. Res.* **47**, 783–792 (2014).
- Beniya, A. & Higashi, S. Towards dense single-atom catalysts for future automotive applications. *Nat. Catal.* **2**, 590–602 (2019).
- Wang, C.-M., Wang, Y.-D., Ge, J.-W. & Xie, Z.-K. Reaction: industrial perspective on single-atom catalysis. *Chem* **5**, 2736–2737 (2019).
- Xiang, H., Feng, W. & Chen, Y. Single-atom catalysts in catalytic biomedicine. *Adv. Mater.* **32**, 1905994 (2020).
- Li, S. et al. Interplay between the spin-selection rule and frontier orbital theory in O₂ activation and CO oxidation by single-atom-sized catalysts on TiO₂(110). *Phys. Chem. Chem. Phys.* **18**, 24872–24879 (2016).
- Fu, Z., Yang, B. & Wu, R. Understanding the activity of single-atom catalysis from frontier orbitals. *Phys. Rev. Lett.* **125**, 156001 (2020).
- Spivey, T. D. & Holewinski, A. Selective interactions between free-atom-like d-states in single-atom alloy catalysts and near-frontier molecular orbitals. *J. Am. Chem. Soc.* **143**, 11897–11902 (2021).
- Ren, Y. et al. Unraveling the coordination structure–performance relationship in Pt/Fe₂O₃ single-atom catalyst. *Nat. Commun.* **10**, 4500 (2019).
- Wang, L. et al. Boosting activity and stability of metal single-atom catalysts via regulation of coordination number and local composition. *J. Am. Chem. Soc.* **143**, 18854–18858 (2021).
- Wang, Y. et al. CO oxidation on Au/TiO₂: condition-dependent active sites and mechanistic pathways. *J. Am. Chem. Soc.* **138**, 10467–10476 (2016).
- Zhou, X. et al. Unraveling charge state of supported Au single-atoms during CO oxidation. *J. Am. Chem. Soc.* **140**, 554–557 (2018).
- Camellone, M. F. & Fabris, S. Reaction mechanisms for the CO oxidation on Au/CeO₂ catalysts: activity of substitutional Au³⁺/Au⁺ cations and deactivation of supported Au⁺ adatoms. *J. Am. Chem. Soc.* **131**, 10473–10483 (2009).
- Lang, R. et al. Single-atom catalysts based on the metal–oxide interaction. *Chem. Rev.* **120**, 11986–12043 (2020).
- O’Connor, N. J., Jonayat, A. S. M., Janik, M. J. & Senftle, T. P. Interaction trends between single metal atoms and oxide supports identified with density functional theory and statistical learning. *Nat. Catal.* **1**, 531–539 (2018).
- Campbell, C. T. Electronic perturbations. *Nat. Chem.* **4**, 597–598 (2012).
- Bruix, A. et al. A new type of strong metal–support interaction and the production of H₂ through the transformation of water on Pt/CeO₂(111) and Pt/CeO₂/TiO₂(110) catalysts. *J. Am. Chem. Soc.* **134**, 8968–8974 (2012).
- Yang, J., Li, W., Wang, D. & Li, Y. Electronic metal–support interaction of single-atom catalysts and applications in electrocatalysis. *Adv. Mater.* **32**, 2003300 (2020).
- Chen, C. et al. Zero-valent palladium single-atoms catalysts confined in black phosphorus for efficient semi-hydrogenation. *Adv. Mater.* **33**, 2008471 (2021).
- Chen, Z. et al. Single-atom heterogeneous catalysts based on distinct carbon nitride scaffolds. *Natl. Sci. Rev.* **5**, 642–652 (2018).
- Hammer, B., Morikawa, Y. & Nørskov, J. K. CO chemisorption at metal surfaces and overlayers. *Phys. Rev. Lett.* **76**, 2141–2144 (1996).
- Houk, K. N. Frontier molecular orbital theory of cycloaddition reactions. *Acc. Chem. Res.* **8**, 361–369 (1975).
- Fukui, K. The role of frontier orbitals in chemical reactions (Nobel Lecture). *Angew. Chem. Int. Ed.* **21**, 801–809 (1982).
- Greiner, M. T. et al. Free-atom-like d states in single-atom alloy catalysts. *Nat. Chem.* **10**, 1008–1015 (2018).
- George, S. M. Atomic layer deposition: an overview. *Chem. Rev.* **110**, 111–131 (2010).
- Jacobsson, T. J. & Edvinsson, T. Photoelectrochemical determination of the absolute band edge positions as a function of particle size for ZnO quantum dots. *J. Phys. Chem. C* **116**, 15692–15701 (2012).
- Xu, H.-Q. et al. Visible-light photoreduction of CO₂ in a metal–organic framework: boosting electron–hole separation via electron trap states. *J. Am. Chem. Soc.* **137**, 13440–13443 (2015).
- Linsebigler, A. L., Lu, G. & Yates, J. T. Jr Photocatalysis on TiO₂ surfaces: principles, mechanisms, and selected results. *Chem. Rev.* **95**, 735–758 (1995).
- Lear, T. et al. The application of infrared spectroscopy to probe the surface morphology of alumina-supported palladium catalysts. *J. Chem. Phys.* **123**, 174706 (2005).
- Davidson, E. R., Kunze, K. L., Machado, F. B. C. & Chakravorty, S. J. The transition metal–carbonyl bond. *Acc. Chem. Res.* **26**, 628–635 (1993).
- Borodzinski, A. & Bond, G. C. Selective hydrogenation of ethyne in ethene-rich streams on palladium catalysts. Part 1. Effect of changes to the catalyst during reaction. *Catal. Rev. Sci. Eng.* **48**, 91–144 (2006).

34. Hu, M. et al. 50 ppm of Pd dispersed on Ni(OH)₂ nanosheets catalyzing semi-hydrogenation of acetylene with high activity and selectivity. *Nano Res.* **11**, 905–912 (2017).
35. Pei, G. X. et al. Ag alloyed Pd single-atom catalysts for efficient selective hydrogenation of acetylene to ethylene in excess ethylene. *ACS Catal.* **5**, 3717–3725 (2015).
36. Kumar, G., Lau, S. L. J., Krcha, M. D. & Janik, M. J. Correlation of methane activation and oxide catalyst reducibility and its implications for oxidative coupling. *ACS Catal.* **6**, 1812–1821 (2016).
37. Zhang, W. et al. Size dependence of Pt catalysts for propane dehydrogenation: from atomically dispersed to nanoparticles. *ACS Catal.* **10**, 12932–12942 (2020).
38. Gorin, D. J., Sherry, B. D. & Toste, F. D. Ligand effects in homogeneous Au catalysis. *Chem. Rev.* **108**, 3351–3378 (2008).
39. Glendening, E. D., Landis, C. R. & Weinhold, F. NBO 7.0: new vistas in localized and delocalized chemical bonding theory. *J. Comput. Chem.* **40**, 2234–2241 (2019).
40. Tran, K. & Ulissi, Z. W. Active learning across intermetallics to guide discovery of electrocatalysts for CO₂ reduction and H₂ evolution. *Nat. Catal.* **1**, 696–703 (2018).

Publisher's note Springer Nature remains neutral with regard to jurisdictional claims in published maps and institutional affiliations.

Springer Nature or its licensor (e.g. a society or other partner) holds exclusive rights to this article under a publishing agreement with the author(s) or other rightsholder(s); author self-archiving of the accepted manuscript version of this article is solely governed by the terms of such publishing agreement and applicable law.

© The Author(s), under exclusive licence to Springer Nature Limited 2025, corrected publication 2025

Methods

Preparation of the SiO₂ sphere substrate

SiO₂ spheres were prepared by the Stöber method⁴¹. Typically, 17.8 ml of ethyl silicate (TEOS), 5.4 ml of NH₃·H₂O, 360 ml of C₂H₅OH and 30 ml of H₂O were added to a 500-ml beaker, and then, the solution mixtures were vigorously stirred at 25 °C for 24 h. Afterwards, the precipitate was centrifuged, washed with ethanol several times and dried at 70 °C overnight. Finally, the SiO₂ spheres were obtained by calcination at 800 °C under 10% O₂/Ar at a flow rate of 40 ml min⁻¹ for 5 h in a tube furnace.

Preparation of MgAl_xO_y and ZnAl_xO_y spinel supports

MgAl₂O_x spinel support was prepared by the coprecipitation method^{42,43}. First, 3.85 g of Mg(NO₃)₂·6H₂O and 11.25 g of Al(NO₃)₃·9H₂O (molar ratio of Mg/Al = 0.5) were dissolved in 100 ml of deionized water at room temperature. Next, NH₃·H₂O was added dropwise to the mixed solution to adjust the pH value to 10 ± 0.5. The resulting suspension was vigorously stirred for 2 h and aged for another 2 h at 65 °C. After that, the precipitate was filtered, washed several times with deionized water, and then dried at 100 °C for 12 h. Finally, the precipitate was calcined at 800 °C for 5 h in a static air atmosphere to obtain MgAl₂O_x spinel. MgAl_xO_y with different ratios of Al to Mg were achieved by varying the amounts of Mg(NO₃)₂·6H₂O and Al(NO₃)₃·9H₂O during the synthesis process. The ZnAl_xO_y spinel support was synthesized using a similar procedure, except that Mg(NO₃)₂·6H₂O was replaced by Zn(NO₃)₂·6H₂O (ref. 44).

Preparation of MO_x nanoparticle supports

MO_x particles were fabricated on an SiO₂ sphere substrate using ALD, which was performed in a viscous flow reactor (ALD-V401-PRO, ACME (Beijing) Technology) with an ultrahigh purity N₂ carrier gas at a flow rate of 200 ml min⁻¹ at a base pressure of 0.6 torr. The size of the MO_x nanoparticles was tuned by varying the number of ALD cycles and deposition temperatures.

ZnO ALD was carried out using DEZ and H₂O as precursors. The DEZ and H₂O precursors were kept at room temperature. The ALD timing sequences were 100 s, 400 s, 140 s and 400 s for the DEZ exposure time, N₂ purge time, H₂O exposure time and N₂ purge time, respectively. ZnO ALD was performed on the SiO₂ sphere substrate at 100 °C for 1, 2 and 3 cycles to obtain the ZnO-1.9 nm, ZnO-2.8 nm and ZnO-4.3 nm samples, respectively. ZnO-8.5 nm was obtained by performing ZnO ALD for 5 cycles at 150 °C.

TiO₂ ALD was carried out using TTIP and H₂O as precursors. The TTIP precursor was heated to 65 °C to obtain sufficient vapour pressure, and H₂O was kept at room temperature. The ALD timing sequences were 60 s, 300 s, 80 s and 300 s for the TTIP exposure time, N₂ purge time, H₂O exposure time and N₂ purge time, respectively. To obtain the TiO₂-1.6 nm and TiO₂-film samples, TiO₂ ALD was performed on the SiO₂ sphere substrate at 150 °C for 1 and 5 cycles, respectively.

Ga₂O₃ ALD was carried out using Ga(CH₃)₃ and H₂O as precursors, which were all kept at room temperature. The ALD timing sequences were 0.01 s, 480 s, 100 s and 480 s for the Ga(CH₃)₃ exposure time, N₂ purge time, H₂O exposure time and N₂ purge time, respectively. To obtain the Ga₂O₃-1.3 nm and Ga₂O₃-film samples, Ga₂O₃ ALD was performed on the SiO₂ sphere substrate at 150 °C for 1 and 10 cycles, respectively.

CoO_x ALD was carried out using CoCp₂ and O₃ as precursors. The CoCp₂ precursor was heated to 90 °C to obtain a sufficient vapour pressure. The ALD timing sequences were 200 s, 300 s, 200 s and 300 s for the CoCp₂ exposure time, N₂ purge time, O₃ exposure time and N₂ purge time, respectively. To obtain the CoO_x-1.4 nm, CoO_x-1.6 nm, CoO_x-1.9 nm, CoO_x-2.6 nm and CoO_x-3.5 nm samples, CoO_x ALD was performed on the SiO₂ sphere substrate at 200 °C for 1, 3, 5, 10 and 20 cycles, respectively.

NiO_x ALD was carried out using NiCp₂ and O₃ as precursors. The NiCp₂ precursor was heated to 90 °C to obtain a sufficient vapour pressure.

The ALD timing sequences were 100 s, 300 s, 100 s and 300 s for the NiCp₂ exposure time, N₂ purge time, O₃ exposure time and N₂ purge time, respectively. To obtain the NiO_x-1.8 nm and NiO_x-7.1 nm samples, NiO_x ALD was performed on the SiO₂ sphere substrate at 150 °C for 1 and 10 cycles, respectively.

InO_x ALD was carried out using In(CH₃)₃ and H₂O as precursors. The In(CH₃)₃ precursor was heated to 60 °C to obtain a sufficient vapour pressure, whereas H₂O was kept at room temperature. The ALD timing sequences were 300 s, 480 s, 300 s and 480 s for the In(CH₃)₃ exposure time, N₂ purge time, H₂O exposure time and N₂ purge time, respectively. To obtain the InO_x-1.3 nm, InO_x-4.5 nm and InO_x-film samples, InO_x ALD was performed on the SiO₂ sphere substrate at 150 °C for 1, 5 and 10 cycles, respectively.

Preparation of Pd_y/MO_x-y nm SACs

Pd_y/MO_x-y nm SACs were fabricated by depositing Pd exclusively on MO_x nanoparticles but not on the SiO₂ sphere substrate using Pd ALD at 150 °C in the same ALD reactor using Pd(hfac)₂ and formalin as precursors. The Pd(hfac)₂ precursor was heated to 65 °C to obtain a sufficient vapour pressure. After temperature stabilization, one cycle of Pd ALD was conducted to prepare the Pd SACs. The ALD timing sequences were 30 s, 200 s, 30 s and 200 s for the Pd(hfac)₂ exposure time, N₂ purge time, formalin exposure time and N₂ purge time, respectively. The resulting samples were denoted as Pd_y/MO_x-y nm (where y represents the size of MO_x). Pd ALD was also carried out on the bare SiO₂ spherical substrate under the same conditions to confirm the selective deposition of MO_x nanoparticles.

Preparation of Pd_y/MO_x-bulk and Pd_y/MO_x SACs

The synthesis of Pd_y single atoms on conventional oxide and sulfide supports was similar to the above procedure of Pd_y/MO_x-y nm synthesis. The ZrO₂, SrTiO₃ and Fe₃O₄ supports were calcined at 800 °C under 10% O₂/Ar at a flow rate of 40 ml min⁻¹ for 5 h in a tube furnace before Pd ALD. The remaining samples, ZnO-bulk, CoO_x-bulk, NiO_x-bulk, InO_x-bulk, MgAl_xO_y, ZnAl_xO_y and Fe₃O₄, were all directly used for Pd ALD without pretreatment.

Characterization

The metal loadings of Pd SACs were determined by an inductively coupled plasma atomic emission spectrometer (ICP-AES, iCAP7400, Thermo Fisher); therein, all the samples were dissolved in hot aqua regia. The XRD patterns were measured in the range of 10–80° on an X-ray diffractometer (TTR-III, Rigaku, Japan) equipped with graphite monochromatized Cu K α radiation ($\lambda = 1.54,178 \text{ \AA}$). AC-HAADF-STEM images were recorded on a JEM ARM200F (JEOL) thermal-field emission microscope with a probe Cs-corrector operating at 200 kV. For the HAADF images, a convergence angle of about 23 mrad and a collection angle range of about 68–174 mrad were used for incoherent atomic number imaging. The MO_x size distribution was obtained by counting more than 200 MO_x nanoparticles from the STEM images at different locations using ImageJ software. The optical absorption and band gap energy of the sample at RT were characterized by an ultraviolet-visible (UV-Vis) spectrophotometer (Shimadzu DUV-3700).

Mott–Schottky plot measurements were performed on a Zahner Zennium electrochemical workstation in a standard three-electrode system. The catalyst supports (20 mg) were first dispersed into a solution of 5 wt% Nafion (10 μl) and ethanol (1 ml). Then, the catalyst support suspension above (30 μl) was dropped onto the surface of the glassy carbon electrode (diameter = 5 mm) to obtain the working electrode. A Pt plate was used as the counterelectrode, and Ag/AgCl served as the reference electrode. A 0.1 M Na₂SO₄ aqueous solution was used as the electrolyte. The frequencies of the Mott–Schottky plot measurements were set as 300 Hz, 500 Hz, 1,000 Hz and 1,500 Hz. The LUMO position of the semiconductor is approximately equal to the flat-band potential determined by Mott–Schottky plots. Notably, there were

trivial structural changes after the Mott–Schottky plot measurements (Supplementary Fig. 10).

In situ diffuse reflectance infrared Fourier transform spectroscopy (DRIFTS) of CO chemisorption was performed on a Nicolet iS10 spectrometer equipped with a mercury cadmium telluride detector and a low-temperature reaction chamber (Praying Mantis Harrick). All samples were first reduced at 100 °C in situ for 30 min under 10% H₂/Ar with a flow rate of 20 ml min⁻¹. Then, the sample was cooled to 25 °C in Ar, and a background spectrum was taken before the catalyst was exposed to 10% CO/Ar at a flow rate of 25 ml min⁻¹ for 20 min until saturation. Subsequently, the catalyst was purged with pure Ar for 20 min to remove the gas phase CO, and the DRIFT spectrum was collected with 256 scans at a resolution of 4 cm⁻¹.

X-ray absorption spectroscopy (XAS) at the Pd K-edge (24.35 keV) was performed at the beamline of the Materials Research Collaborative Access Team at Sector 10 of the Advanced Photon Source, Argonne National Laboratory. The Athena software package was used for the data analysis.

In situ XPS experiments were performed on a ThermoFisher instrument (ESCALAB XI+) equipped with a gas cell (Model HPGC 300, Fermi Instruments) directly mounted to the sample chamber at the Dalian Institute of Chemical Physics. The spectra were recorded using monochromated X-ray irradiation with Al K α ($h\nu = 1,486.7$ eV) as the X-ray source. After reduction in 10% H₂/Ar (the flow rate was 20 ml min⁻¹ and the total pressure was 1 bar) at 100 °C for 30 min in the high-pressure gas cell, the sample was directly transferred to the analysis chamber in UHV without exposure to air. All XPS spectra were recorded at room temperature under UHV conditions (about 5×10^{-10} mbar) and calibrated for the charging effect by considering the C1s peak at 284.6 eV and the Si 2p peak at 103.5 eV.

Ultraviolet photoelectron spectroscopy measurements were performed in a Thermo Scientific ESCALAB 250Xi instrument using a He discharge lamp (He: $h\nu = 21.22$ eV). The data were acquired with a -10 eV bias during the ultraviolet photoelectron spectroscopy measurements, and Au foil (Alfa Aesar, 99.999%) was used as a reference. The work functions (ϕ) and HOMO and LUMO positions of these samples were calculated based on equations (1–3), respectively,

$$\phi = 21.22 \text{ eV} - (E_{\text{cutoff}} - E_F) \quad (1)$$

$$\text{HOMO position(vacuum level)} = -(VB - E_F + \phi) \quad (2)$$

$$\begin{aligned} \text{LUMO position(vacuum level)} \\ = \text{HOMO position(vacuum level)} + E_g \end{aligned} \quad (3)$$

where the Fermi edge (E_F) starts at the cut-off of photoemission spectra near zero binding energy. The secondary electron emission cut-off energy (E_{cutoff}) was calculated by the extremum in the first-order differential cut-off region. The valence band edge (VB) was calculated by the crossover point between the tangent of the photoemission spectra and the x-axis⁴⁵. The band gap (E_g) was determined by UV–Vis spectroscopy.

TPD of acetylene and H₂ was conducted on a Micromeritics Auto-Chem II chemisorption instrument connected to an online mass spectrometer (Pfeiffer OmniStar). Before the TPD measurements, all the samples were first reduced at 100 °C for 30 min under 10% H₂/Ar at a flow rate of 20 ml min⁻¹. Next, the sample was cooled to 10 °C in He, and C₂H₂ was introduced to the sample for 30 min to ensure saturated adsorption. Subsequently, the sample was purged with He for 1 h to remove the weakly bonded and physically adsorbed C₂H₂ on the sample. Next, the sample was gradually heated from 10 °C to 300 °C in He at a rate of 10 °C min⁻¹, and the C₂H₂ signal ($m/z = 26$) was recorded by mass spectrometry. The procedure of H₂ TPD was similar to that of C₂H₂ TPD, except that C₂H₂ was replaced by H₂ and the temperature range of TPD was changed to 0–500 °C.

In situ thermogravimetric analysis measurements were performed on a TGA550 instrument (TA Instruments) equipped with an evolved gas analysis furnace to quantify coke formation during the semi-hydrogenation of acetylene. The sample was placed in an alumina crucible and heated at a rate of 3 °C min⁻¹ in 10% H₂/Ar (20 ml min⁻¹) from room temperature to 100 °C and kept for 30 min. Next, the sample was purged with Ar for 15 min before cooling to 80 °C. Then, the acetylene hydrogenation reaction gas, consisting of 1% acetylene, 2% H₂ and 50% ethylene with Ar as the balance gas, was introduced to the reactor for 25 h. The evolution of the sample weight during acetylene hydrogenation was then recorded.

Catalyst evaluation

The semi-hydrogenation of acetylene in excess ethylene was carried out in a fixed-bed quartz tube reactor at atmospheric pressure. The amounts of Pd_x/MO_y catalysts were adjusted to maintain the same Pd content. The sample was diluted with 1.0 g of 60–80 mesh quartz chips to avoid any hot spots. Before the reaction test, all catalysts were reduced in situ in 10% H₂/Ar at 100 °C for 30 min. Then, reaction feed gas, consisting of 1% acetylene, 2% H₂ and 50% ethylene with Ar as the balance gas, was introduced into the catalyst bed at a flow rate of 20 ml min⁻¹. The reaction products were analysed using an online gas chromatograph (Shimadzu GC-2014) equipped with a flame ionization detector and a capillary column (Rt-Alumina BOND/Na₂SO₄, 50 m × 0.53 mm). The acetylene conversion, ethylene selectivity and TOF were calculated using equations (4–6), respectively:

$$C_2H_2 \text{ conversion} = \left(\frac{[C_2H_2]_{\text{in}} - [C_2H_2]_{\text{out}}}{[C_2H_2]_{\text{in}}} \right) \times 100\% \quad (4)$$

$$C_2H_4 \text{ selectivity} = \left(1 - \frac{[C_2H_4]_{\text{out}}}{[C_2H_2]_{\text{in}} - [C_2H_2]_{\text{out}}} \right) \times 100\% \quad (5)$$

$$TOF = \frac{[C_2H_2]_{\text{in}} \times C_2H_2 \text{ conversion}}{n_{\text{Pd}} \times 100\% \times 22.4 \times 10^{-3}} \quad (6)$$

Here, [C₂H₂]_{in} and [C₂H₂]_{out} are the concentrations of acetylene at the inlet and outlet of the reactor, respectively; [C₂H₄]_{out} is the concentration of ethane at the outlet of the reactor; and n_{Pd} is the mole of Pd content. The molar volume of gas under standard conditions is 22.4×10^{-3} ml mol⁻¹.

Selective hydrogenation of 1,3-butadiene was also performed in a fixed-bed quartz tube reactor at atmospheric pressure. The reaction feed gas of the acetylene mixture gas was replaced by a mixture of 1,3-butadiene gas, which consisted of 1% 1,3-butadiene and 2% H₂ with Ar as the balance gas. The 1,3-butadiene conversion and butylene selectivity were calculated using equations (7) and (8), respectively:

$$C_4H_6 \text{ conversion} = \left(\frac{[C_4H_6]_{\text{in}} - [C_4H_6]_{\text{out}}}{[C_4H_6]_{\text{in}}} \right) \times 100\% \quad (7)$$

$$C_4H_8 \text{ selectivity} = \left(1 - \frac{[C_4H_8]_{\text{out}}}{[C_4H_6]_{\text{in}} - [C_4H_6]_{\text{out}}} \right) \times 100\% \quad (8)$$

Here [C₄H₆]_{in} and [C₄H₆]_{out} are the concentrations of 1,3-butadiene at the inlet and outlet of the reactor, respectively; [C₄H₈]_{out} is the concentration of butane at the outlet of the reactor.

Kinetic measurements

Kinetic measurements were further performed in the same fixed-bed reactor. The amount of Pd catalyst was reduced to maintain the acetylene conversion below 20%. The apparent activation energies were determined on the same reaction system in the temperature range

Article

between 60 °C and 120 °C with the same feed gas composition used for acetylene hydrogenation. To measure the H₂ reaction order, we kept the concentration of acetylene constant at 1% while changing the H₂ concentration from 2% to 9%. To measure the C₂H₂ reaction order, we kept the concentration of H₂ constant at 6% while changing the C₂H₂ concentration from 1% to 3%.

H-D exchange reaction

The H–D exchange reaction was carried out in a fixed-bed quartz tube reactor at atmospheric pressure. The catalyst was diluted with 1 g of fine quartz chips, and the amount of catalyst was adjusted to keep the H₂ conversion below 20%. Before the H–D exchange reaction test, the sample was first reduced in 10% H₂/Ar at 100 °C for 30 min. Next, a feed gas consisting of 10% D₂ and 10% H₂ with Ar as the balance gas was introduced to the sample at a total flow rate of 20 ml min⁻¹. The reaction temperature was varied from 60 °C to 120 °C. The signals of H₂ (*m/z* = 2), HD (*m/z* = 3) and D₂ (*m/z* = 4) were recorded by online mass spectrometry (Pfeiffer OmniStar). The HD exchange activity and kinetic data were also calculated in the same way as those for acetylene hydrogenation.

DFT calculations

All computations were carried out using the spin-polarized DFT method implemented in the Vienna ab initio Simulation Package (ref. 46). The projector-augmented-wave pseudopotential was used to treat the core electrons, whereas the Perdew–Burke–Ernzerhof exchange-correlation functional of the generalized gradient approximation (GGA) was used to describe the electron interactions^{47–50}. Considering the systemic error of the GGA functional for describing the electronic structure of transition metal oxides, it is worth noting that the absolute energy level positions of the LUMO mentioned in the article might not be very accurate, whereas the trend of the energy-level position change with size can be informative and is what we are truly concerned with. A plane-wave cut-off energy of 500 eV was adopted for all calculations and both lattice constants along the periodic direction and atomic positions were optimized with the convergence of energy and force less than 10⁻⁵ eV and |0.05| eV Å⁻¹, respectively. The van der Waals interactions were described using the empirical correction in Grimme's scheme⁵¹. The study of charge transfer was completed by Bader charge analysis⁵². The adsorption energy of a gas molecule is defined as $E_{\text{ads}} = E_{\text{mol}^*} - E_{\text{mol}} - E^*$, where E_{mol} , E^* and E_{mol^*} are the total energies of the gas molecule, the Pd₁SAC and the adsorbate/SAC system, respectively. Moreover, the free energies of the reactant, product and reaction intermediates are defined as $G = E_{\text{DFT}} + E_{\text{ZPE}} - TS$, where E_{DFT} , E_{ZPE} and TS represent the DFT-calculated electronic energy, zero-point energy and entropy of the system, respectively. The calculated finite-temperature entropy and zero-point energy (ZPE) are listed in Supplementary Table 12. The climbing image nudged elastic band (CI-NEB) method⁵³ was used to calculate the reaction activation energy barriers, with the transition states verified through a rigorous vibrational frequency analysis.

For the catalyst model, considering the consumption of computing resources and experimental characterization results, a series of approximately pie-shaped ZnO clusters (named ZnO-*x*, where *x* is the number of ZnO units in the chemical formula) mainly exposed to the (1010) surface was constructed to simulate different sizes of support particles. The ZnO-52 support, which has similar sizes to the experimental 1.9 nm particle, was selected as the model for the specific calculation of the reaction. The largest support was modelled by a (3 × 2) supercell of a seven-atomic-layer ZnO(1010) surface (named ZnO-slab), and the bottom three layers of atoms were fixed during optimization. A vacuum layer of more than 15 Å for all the models was used to avoid interactions between periodically repeated structures. Zinc vacancies on the ZnO surface were selected as the anchor sites for a single Pd atom, as shown in Supplementary Table 8.

Natural resonance theory analysis was conducted by using the Natural Bond Orbital (NBO 7.0) and Gaussian16 program package to evaluate the ionicity of surface Pd–O chemical bonds on various oxide supports^{54–56}.

Microkinetic simulations

Microkinetic simulations were performed by using the MKMCXX program^{57,58}. The contributions of the elementary steps to the overall reaction were determined through the degree of rate control method⁵⁹. For acetylene hydrogenation to ethylene from 340 K to 370 K on Pd₁/ZnO-52 and Pd₁/ZnO-slab, the gas phase contains a mixture of C₂H₂ and H₂ in a 1:2 molar ratio at a total pressure of 0.1 MPa, similar to the experimental conditions. For Pd₁/ZnO-52, a gas phase with and without the presence of C₂H₄ (C₂H₂:H₂:C₂H₄ = 1:2:0 and C₂H₂:H₂:C₂H₄ = 1:2:10) was adopted to consider the impact of C₂H₄ on the reaction kinetics. The reaction rates of each elementary reaction were calculated based on the surface coverages of the steady state. The reaction pathways, including the dissociation of H₂, C₂H₂* hydrogenation to C₂H₃*, followed by C₂H₃* to C₂H₄* and the kick-off of C₂H₄* by C₂H₂, were all considered in the kinetic calculations.

Data availability

All data generated during this study are included in this published article (and Supplementary Information) or can be obtained from the authors upon reasonable request. Source data are provided with this paper.

41. Bourgeat-Lami, E. & Lang, J. Encapsulation of inorganic particles by dispersion polymerization in polar media: 2. effect of silica size and concentration on the morphology of silica-polystyrene composite particles. *J. Colloid Interface Sci.* **210**, 281–289 (1998).
42. Guo, J. et al. Dry reforming of methane over nickel catalysts supported on magnesium aluminate spinels. *Appl. Catal. A Gen.* **273**, 75–82 (2004).
43. Theofanidis, S. A., Galvita, V. V., Poelman, H. & Marin, G. B. Enhanced carbon-resistant dry reforming Fe-Ni catalyst: role of Fe. *ACS Catal.* **5**, 3028–3039 (2015).
44. Cornu, L., Gaudon, M. & Jubera, V. ZnAl₂O₄ as a potential sensor: variation of luminescence with thermal history. *J. Mater. Chem. C* **1**, 5419–5428 (2013).
45. Zhang, J. et al. Deep UV transparent conductive oxide thin films realized through degenerately doped wide-bandgap gallium oxide. *Cell Rep. Phys. Sci.* **3**, 100801 (2022).
46. Kresse, G. & Furthmüller, J. Efficient iterative schemes for ab initio total-energy calculations using a plane-wave basis set. *Phys. Rev. B* **54**, 11169–11186 (1996).
47. Kresse, G. & Joubert, D. From ultrasoft pseudopotentials to the projector augmented-wave method. *Phys. Rev. B* **59**, 1758–1775 (1999).
48. Blöchl, P. E. Projector augmented-wave method. *Phys. Rev. B* **50**, 17953–17979 (1994).
49. Perdew, J. P., Burke, K. & Ernzerhof, M. Generalized gradient approximation made simple. *Phys. Rev. Lett.* **77**, 3865–3868 (1996).
50. Maintz, S., Deringer, V. L., Tchougréff, A. L. & Dronskowsk, R. Analytic projection from plane-wave and PAW wavefunctions and application to chemical-bonding analysis in solids. *J. Comput. Chem.* **34**, 2557–2567 (2013).
51. Grimme, S., Ehrlich, S. & Goerigk, L. Effect of the damping function in dispersion corrected density functional theory. *J. Comput. Chem.* **32**, 1456–1465 (2011).
52. Henkelman, G., Arnaldsson, A. & Jónsson, H. A fast and robust algorithm for Bader decomposition of charge density. *Comp. Mater. Sci.* **36**, 354–360 (2006).
53. Henkelman, G., Uberuaga, B. P. & Jónsson, H. A climbing image nudged elastic band method for finding saddle points and minimum energy paths. *J. Chem. Phys.* **113**, 9901–9904 (2000).
54. Reed, A. E., Curtiss, L. A. & Weinhold, F. Intermolecular interactions from a natural bond orbital, donor-acceptor viewpoint. *Chem. Rev.* **88**, 899–926 (1988).
55. Gaussian 16, Revision C.01 (Theoretical Chemistry Institute, Univ. Wisconsin, 2018).
56. Glendening, E. D. & Weinhold, F. Natural resonance theory: I. General formalism. *J. Comput. Chem.* **19**, 593–609 (1998).
57. Filot, I. A. W., van Santen, R. A. & Hensen, E. J. M. The optimally performing Fischer–Tropsch catalyst. *Angew. Chem. Int. Ed.* **53**, 12746–12750 (2014).
58. Filot, I. A. W. et al. First-principles-based microkinetics simulations of synthesis gas conversion on a stepped rhodium surface. *ACS Catal.* **5**, 5453–5467 (2015).
59. Stegemann, C., Andreassen, A. & Campbell, C. T. Degree of rate control: how much the energies of intermediates and transition states control rates. *J. Am. Chem. Soc.* **131**, 8077–8082 (2009).

Acknowledgements This work was supported by the National Key R&D Program of China (2021YFA1502802), the Chinese Academy of Sciences (XDA29040800), the National Science Fund for Distinguished Young Scholars (2022505 and 22225301), the National Science Fund of China (22221003, 22073087, 22302200, 22321001 and 22472164), the NSFC Center for Single-Atom Catalysis (22388102), the Fundamental Research Funds for the Central Universities (WK2060000038 and 20720220009), the Strategic Priority Research Program of the CAS (XDB0450101), K. C. Wong Education (GJTD-2020-15), the CAS Project for Young Scientists in

Basic Research (YSBR-022 and YSBR-004), the Dalian Institute of Chemical Physics (DICP I202107), the Innovation Program for Quantum Science and Technology (2021ZD0303302) and the National Science Foundation Graduate Research Fellowship under grant no. 2234662. Z.F. also acknowledges the support of the China Experience Fund from Oregon State University. XAS experiments were performed at the 10-ID of the Materials Research Collaborative Access Team, which is supported by the US Department of Energy (DOE) and the Materials Research Collaborative Access Team member institutions. This research used the resources of the Advanced Photon Source, a US DOE Office of Science User Facility operated for the DOE Office of Science by Argonne National Laboratory under contract no. DE-AC02-06CH11357. We also thank J. Yang, J. Liu and L. Feng for their comments and S. Han, L. Xu and L. Cai for providing catalytic support.

Author contributions J.L. conceived the project and designed the experiments; X.S., H.W., J.D., S.C., W.X. and Y. Li performed the catalytic performance evaluation; X.W., H.L. and Z.W. performed the theoretical calculations; Q.G., X.X., Y. Lin, P.D., T.Z. and B.Y. carried out the

STEM and XPS measurements; M.S. performed the ICP measurements; X.S., L.J. and H.-L.J. conducted the Mott–Schottky curve measurements; M.P.L., A.C. and Z.F. carried out the XAS measurements; J.L., X.S., Q.G., B.Y., X.W. and Z.W. wrote the paper. All the authors contributed to the overall scientific interpretation and edited the paper.

Competing interests The authors declare no competing interests.

Additional information

Supplementary information The online version contains supplementary material available at <https://doi.org/10.1038/s41586-025-08747-z>.

Correspondence and requests for materials should be addressed to Bing Yang, Xiaojun Wu or Junling Lu.

Peer review information *Nature* thanks Thomas Senftle and the other, anonymous, reviewer(s) for their contribution to the peer review of this work. Peer reviewer reports are available.

Reprints and permissions information is available at <http://www.nature.com/reprints>.